Three-dimensional injection molding simulation of AZ91D semi-solid magnesium alloy

Ilinca, Florin; Hétu, Jean-Francois; Moisan, Jean-Francois; Ajersch, Frank

Publisher's version / Version de l'éditeur:
https://doi.org/10.1007/s12289-008-0005-4
International Journal of Material Forming, 1, March 1, pp. 3-12, 2008

2007-117031-G
CNRC-49660

Noname manuscript No.
(will be inserted by the editor)

Three-dimensional Injection Molding Simulation of AZ91D Semi-Solid Magnesium Alloy

Florin Ilinca · Jean-François Hétu · Jean-François Moisan · Frank Ajersch

Received: date / Accepted: date

Abstract Magnesium alloys are increasingly used in automotive, aeronautic and electronic applications to produce high performance, light weight parts. In the thixomolding process a semi-solid slurry is injected into a mold at controlled temperature such that the melt has specific flow behavior. This allows the fabrication of near net shape components with controlled microstructure and good mechanical properties. The numerical modeling of such applications present unusual challenges for both the physical modelling and the solution algorithm. This paper presents a 3D numerical solution algorithm for the simulation of the injection molding of semi-solid AZ91 magnesium alloys. The methodology deals with the shear thinning, temperature dependent viscosity behavior and is able to accurately solve the high velocity flows encountered during semi-solid magnesium molding. A segregated algorithm is used to solve the Navier-Stokes, energy and front tracking equations. The position of the flow front in the mold cavity is computed using a level set approach. Equations are integrated in time using an implicit Euler scheme and solved by stabilized finite element methods. The approach is applied to the injection of a tensile bar and the results compared with experimental

F. Ilinca
National Research Council, 75 de Mortagne, Boucherville, Qc, Canada, J4B 6Y4
Tel.: +450-641-5072
Fax: +450-641-5104
E-mail: florin.ilinca@cnrc-nrc.gc.ca

J.-F. Hétu
National Research Council, 75 de Mortagne, Boucherville, Qc, Canada, J4B 6Y4
Tel.: +450-641-5082
E-mail: jean-francois.hetu@cnrc-nrc.gc.ca

J.-F. Moisan
National Research Council, 75 de Mortagne, Boucherville, Qc, Canada, J4B 6Y4
Tel.: +450-641-5389
E-mail: jean-francois.moisan@cnrc-nrc.gc.ca

F. Ajersch
École Polytechnique de Montréal, C.P. 6079, Succ. Centre-Ville, Montréal, Québec, Canada, H3C 3A7
Tel.: +514-340-4102(4533)
E-mail: frank.ajersch@polymtl.ca

data. The methodology presents the robustness and cost effectiveness needed to tackle complex industrial applications.

Keywords Semi-solid metal · Mold filling · 3D Modeling · Finite Elements · Shear thinning

1 Introduction

The use of magnesium (Mg) alloys in the fabrication of structural and non-structural parts for various industries has grown continuously in the past years. In the automotive industry this growth was driven by the ever increasing demands for reduced vehicle emissions and improved fuel consumption which can be achieved in part by the reduction of vehicle weight [1,2]. The ability to reliably cast components of various shapes and section thickness for structural components could further increase the use of Mg alloys in vehicles. The resulting physical and mechanical properties are very sensitive to the forming process and the rate of solidification. The control of the mold filling and solidification is therefore essential in attaining high integrity parts. The highest rate of solidification is achieved in die casting whereas the lowest rates occur in sand and plaster castings. In semi-solid forming one can combine controlled flow of the slurry having higher viscosity and high solidification rates as a partially solidified material requires less heat extraction [3,4]. In these processes a semi-solid slurry is injected into the mold at controlled temperature such that the melt has specific flow behavior. The alloy chemistry and morphology of the solid particles need also to be controlled in order to achieve a solidified alloy structure that will result in optimal mechanical properties.

The objective of this work is to develop numerical simulation tools for the prediction of the semi-solid metal mold filling. Such applications involve free-surface fluid flow coupled with heat transfer, non constant material properties, and complicated three-dimensional geometries. The flow is at high Reynolds number, on geometries having high aspect ratio components. Strong nonlinear dependence of flow properties on velocity are common place, such as large and rapid spatial variations of the apparent viscosity. The viscosity of semi-solid Mg alloys exhibit important shear thinning and solid fraction dependence. During the injection of complex industrial parts, the semi-solid alloy flows through converging and diverging sections as well as in areas presenting drastic changes in thickness and flow directions. Typical examples of these cases include flow in channels with high aspect ratios, sudden contractions/expansions (gates), ribs, transitions in cavity thickness and flow around corners. In many cases these regions can be the source of molding problems (air entrapment, porosity, etc.) and a more detailed understanding of the flow characteristics in these areas might be useful in solving undesirable situations. Such problems place special demands on the solution algorithm. The technique must be robust and provide accurate solutions for a wide range of parameters. This paper presents a finite element method capable of tackling these difficulties. Similar algorithms were previously used by the authors to solve a variety of molding applications, as die casting [5], polymer injection molding [6], gas-assisted injection molding [7], co-injection [8] and injection of metal powders [9]. This body of work has shown the ability of the solution algorithm to treat a large spectrum of flow regimes ranging from low velocity creeping flow to high velocity turbulent flows, including heat transfer, free surface and multi-phase modeling. The work presented here is an extension to semi-solid metal injection molding. At this point

there are very few published simulation results for the injection molding of semi-solid magnesium [10–12]. Kim *et al.* [10] used the commercial software MAGMA to make 3D computations. They use a power law model to describe the viscosity and obtain almost isothermal flow conditions. Results are shown for 40% and 2% solid fraction on a relatively simple geometry. Lohmüller *et al.* [11] made simulations at constant viscosity and analyzed the influence of the viscosity on the filling pattern.

The paper is organized as follows. First, the equations describing time-dependent laminar flow along with their boundary and initial conditions are presented in Section 2. The rheological behavior of AZ91 alloys in semi-solid state is then discussed. The solution algorithm and the finite element approach are described in Section 3. The transient momentum, continuity, energy and front tracking equations are solved using linear finite elements. The methodology is applied in Section 4 to the simulation of the filling pattern during the injection molding of a tensile bar and the numerical prediction is compared with experimental observation. The paper ends with conclusions.

2 Model equations

2.1 Flow equations

During the filling of the mold, the Mg alloy is considered incompressible and behaving as a generalized Newtonian fluid. The flow is at high Reynolds number and for instant is considered as being laminar. The flow of incompressible fluids is described by the Navier-Stokes equations:

$$\rho\left(\frac{\partial \mathbf{u}}{\partial t} + \mathbf{u}\cdot\nabla\mathbf{u}\right) = -\nabla p + \nabla\cdot\left[2\eta\dot{\gamma}(\mathbf{u})\right], \tag{1}$$

$$\nabla\cdot\mathbf{u} = 0, \tag{2}$$

where t, $\mathbf{u}$, p, ρ and η denote time, velocity, pressure, density and viscosity respectively and $\dot{\gamma} = (\partial u_i/\partial x_j + \partial u_j/\partial x_i)/2$ is the strain rate tensor.

2.2 Rheological model

Several experimental studies were carried out to characterize the rheological behavior of the AZ91D magnesium alloy in the semi-solid state. The measured viscosities indicate large discrepancies between the different studies. The tests performed by Ghosh *et al.* [13] indicate the lowest viscosity, whereas those of Mao *et al.* [14] result in a viscosity about one order of magnitude higher. Measurements of Gebelin *et al.* [15] leads to a viscosity of the slurry three orders of magnitude higher that the one measured by Ghosh *et al.* [13]. All experiments agree on the fact that the slurry has a shear thinning behavior (i.e. the viscosity decreases with increasing shear rate) and depends on the solid fraction. We use here the following expression for the viscosity:

$$\eta = Ae^{Bf_s}\left(\frac{\dot{\gamma}}{\dot{\gamma}_0}\right)^{-n} \tag{3}$$

where A and B are model parameters, n is a positive power law coefficient, f_s is the solid fraction and $\dot{\gamma}_0$ is a reference shear rate defining the scale for the rate of shear.

Table 1 Constants for the rheological model

Case	Measure	n	A ($Pa \cdot s$)	B	$\dot{\gamma}_0$ (s^{-1})	T_s (^0C)	T_m (^0C)	k_0
A	Mao *et al.* [14]	0.87‡	0.8	6.4	200	470	597	0.57
B	Ghosh *et al.* [13]	0.85	24	2†	1	470	595	0.65

‡ $n = n_0(f_s/f_{s0})^{0.3}$; $n_0 = 0.87$, $f_{s0} = 0.68$.
† For $f_s > 0.4$: $B = 2 + 7.5(f_s - 0.4)^2$.

The shear thinning behavior is characterized by the exponential coefficient n of the power-law model. Ghosh *et al.* [13] used a Couette viscometer to perform experiments and found the power-law constant to be equal to 0.85; Gebelin *et al.* [15] used compression (low shear rate) and backward extrusion (high shear rate) experiments and obtained for the exponent n values of 0.65 and 0.95, respectively. Mao *et al.* [14] used a Couette rheometer to investigate the influence of the solid fraction on the power-law coefficient. They found that the power-law coefficient n is approximately 0.84 for a high solid fraction slurry. This result agrees well with the 0.85 value reported by Ghosh *et al.* [13] and the value of 0.87 reported by Gebelin *et al.* [15]. At 580^0C the exponent was found to be 0.67, which is close to the value of 0.65 measured by Gebelin *et al.* [15] in the compression experiment.

The solid fraction at equilibrium depends on the temperature and is given by the Scheil equation:

$$f_s = 1 - \left(\frac{T_s - T}{T_s - T_m}\right)^{\frac{1}{1-k_0}} \tag{4}$$

where T is the alloy temperature, T_s is the freezing temperature, T_m is the liquidus temperature and k_0 is the partition coefficient.

The model constants that lead to a good fit of the experimental data of Mao *et al.* [14] and of Ghosh *et al.* [13] are given in Table 1.

The viscosity dependence on the shear rate for various solid fractions is shown in Figure 1 for the data of Mao *et al.* [14] and in Figure 2 for the model fitting the Ghosh *et al.* [13] data. In both figures the symbols represent the measured apparent viscosity, whereas the lines are the data as from the viscosity model Eq. (3) and the parameters of Table 1. In the data obtained by Mao *et al.* [14] the power law exponent depends on the solid fraction. The experimentally measured power law exponent and the numerical model used in the simulations (see Table 1) are shown in Figure 3. Remark that the viscosity measured by Ghosh is about one order of magnitude smaller than the one obtained by Mao. This discrepency is indicative of the difficulty to characterize the rheological behavior of semi-solid materials. Such materials exhibit thixotropic behavior, in which the viscosity at constant shear depends in time as a result of micro-structural changes. The viscosity depends also on the time at rest before the tests [14,16], it is highly sensitive to the temperature and may be affected by phase segregation. All those phenomena influence the accuracy of the measured viscosity and also determine a level of uncertainty with regard to the actual viscosity of the slurry during the molding. A measure of the viscosity in conditions close to those encountered during mold filling was reported by Yang *et al.* [17]. They used a slit rheometer, on which the material is pushed inside a rectangular plate by means of a plunger. The velocity and shear rate encountered during the test (high shear rate) are similar to those obtained during semi-solid mold filling. They obtain values of the apparent viscosity that are close to

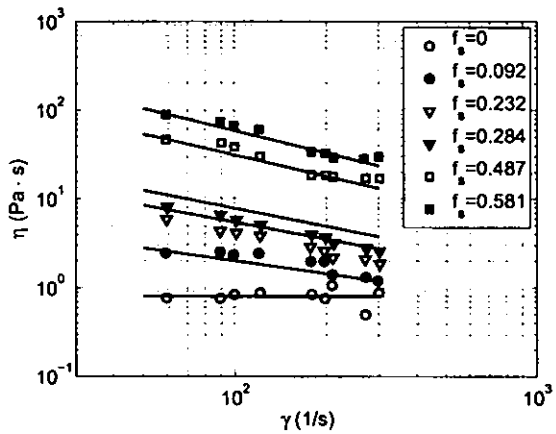

Fig. 1 Viscosity model A from the data of Mao *et al.* [14].

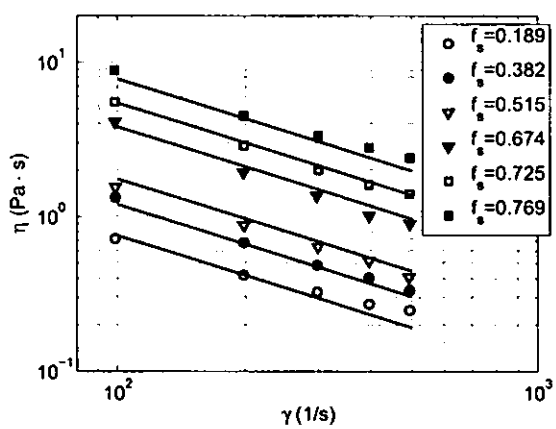

Fig. 2 Viscosity model B from the data of Ghosh *et al.* [13].

those reported by Mao *et al.* [14] as shown in Figure 4. The range of shear rate for which the apparent viscosity was measured is restrained by the fact that at higher plunger speed the measured pressure was affected by flow turbulence in the die cavity, whereas at lower plunger speed the pressure difference was to small to get a reliable viscosity. In the experiment of Yang *et al.* [17] the mold was heated at 300^0C, hence at a temperature below of that of the slurry. This determines non-isothermal effects that may affect the measured viscosity.

Measure of the viscosity of AZ91 magnesium alloys was also reported by Messaoud *et al.* [18] for two moderate values of the shear rate. Experiments were conducted using a Couette type viscometer and the viscosity was monitored as a function of the temperature for a constant cooling rate of $2^0C/min$. The data recovers the same exponential

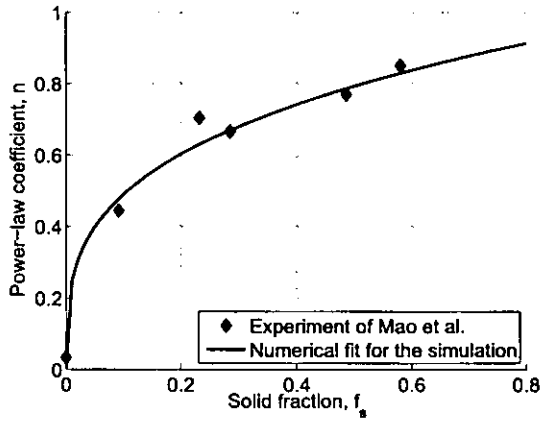

Fig. 3 Viscosity model A: Power law exponent from the data of Mao *et al.* [14].

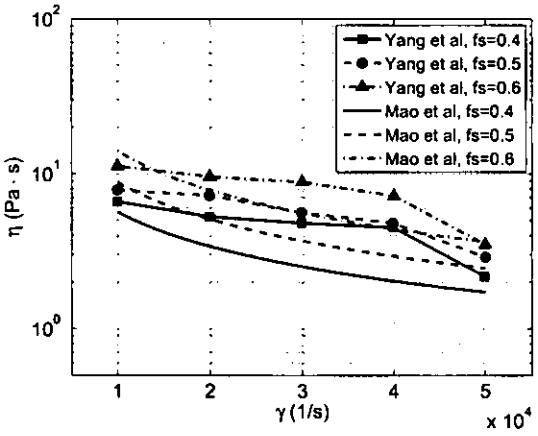

Fig. 4 Apparent viscosity of Yang *et al.* [17] compared with model A.

dependence of the viscosity on the solid fraction, but with an exponential coefficient B depending on the shear rate. The data from Messaoud *et al.* [18] is compared with the models A and B, matching the data of Ghosh *et al.* [13] and of Mao *et al.* [14], in Figure 5. At 580^0C the experiments of Messaoud indicate a viscosity closer to that of Ghosh (model B) especially for the higher shear rate value ($\dot{\gamma} = 104s^{-1}$).

The discrepancies between the measurements of Ghosh *et al.* [13] and of Mao *et al.* [14] may be explained by differences in the methodology followed to obtain the semi-solid slurry and in the state of shear before the beginning of the tests. Mao do not mention if the semi-solid alloy was kept under constant shear or at rest before the experiment, but in the thixomolding experiment of Yang *et al.* [17] the slurry is at rest before being injected into the slit rheometer. Those two experiments result in

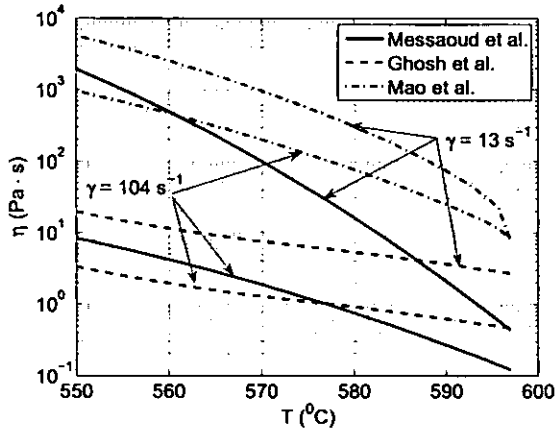

Fig. 5 Apparent viscosity of Messaoud *et al.* [18] compared with models A (Mao *et al.* [14]) and B (Ghosh *et al.* [13]).

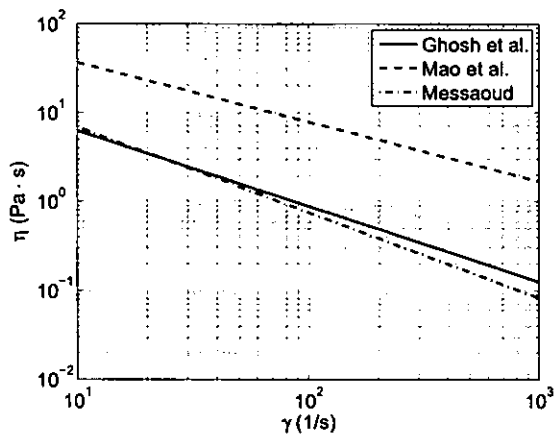

Fig. 6 Apparent viscosity at 580^0C from models A, B and data of Messaoud [19]

a higher apparent viscosity. On the other hand the data of Ghosh was obtained with the semi-solid alloy being maintained at a constant shear rate of $297.3s^{-1}$ before the viscosity tests. Shearing of the material leads to the formation of smaller more uniformly distributed spherical particles. This give rise to lower values of the apparent viscosity in comparison with the case of larger, non-spherical and agglomerated particles found in a slurry maintained at rest. Another experiment on which the slurry was maintained under constant shear of $134s^{-1}$ before being submitted to a sharp change in the shear rate is reported by Messaoud [19]. His data agree well with the viscosity measured by Ghosh for a temperature of 580^0C (see Figure 6). In the present simulation work we have used both the viscosity models from the Mao *et al.* data [14] and from the Ghosh *et al.* data [13] (models A and B in Table 1). The viscosities from the two models at

the injection temperature of 580^0C are compared in Figure 6. In the molding machine, prior to the injection, the slurry is maintained at constant temperature and under shear rate as determined by the rotation of the screw. This conditions are closer to those encountered in the Ghosh's experiment, hence his set of viscosity data is expected to describe better the rheology behavior during the present injection molding application. Ghosh's data B results in a lower viscosity that decreases faster with increasing shear rate.

2.3 Heat transfer

The heat transfer is modeled by the energy equation:

$$\rho c_p \left(\frac{\partial T}{\partial t} + \mathbf{u} \cdot \nabla T \right) = \nabla \cdot (k \nabla T), \tag{5}$$

where T, c_p and k denote temperature, specific heat and conductivity respectively. Because the slurry is injected at a temperature where both solid and liquid phases are present, any change in the temperature is supposed to determine a change in the solid fraction. This is taken into account by considering an effective specific heat that incorporates the effect of the latent heat of fusion:

$$c_p = c_{p0} + \lambda \frac{\mathrm{d}f_s}{\mathrm{d}T} \tag{6}$$

where $c_{p0} = 1050 J/kg \cdot K$ and $\lambda = 3.73 \cdot 10^5 J/kg$. The derivative of the solid fraction with respect to temperature is obtained by differentiating Eq. (4). The density and heat conductivity are $\rho = 1830 kg/m^3$ and $k = 72 W/m \cdot K$ respectively.

2.4 Mold filling simulation

For mold filling applications in addition to solving for the flow equations we have to track in time the position of the interface between the filling material and the air/void inside the cavity. Front tracking is done using a level-set method [5]. For this, a smooth function $F(x,t)$ is introduced such that a pre-determined value, F_c, represents the position of the interface. A value larger than F_c indicates a filled region, whereas in empty regions the front tracking function is smaller than F_c. The front tracking function is transported using the velocity field provided by the solution of the momentum-continuity equations:

$$\frac{\partial F}{\partial t} + \mathbf{u} \cdot \nabla F = 0. \tag{7}$$

2.5 Boundary conditions

The problem definition is completed by imposing boundary conditions. The velocity is imposed on the mold inlet, no-slip boundary conditions are imposed on the cavity walls filled by the suspension and a free boundary condition is considered on the unfilled part. For heat transfer, the temperature is set on the inlet, an adiabatic conditions is

imposed on the symmetry planes, while the heat flux between the cavity and the filled part of the mold is given by

$$q_m = h_c (T - T_m) \quad \text{on } \Gamma_{mold}. \tag{8}$$

where h_c is a surface heat transfer coefficient and T_m is the mold temperature.

3 Finite element solution

Model equations are discretized in time using a first order implicit Euler scheme. Linear continuous shape functions are used for all variables. At each time step, the global system of equations is solved in a partly segregated manner. The solution algorithm solves separately the systems of equations as follows:

```
For time smaller than the filling time:
1. Solve the incompressible momentum-continuity equations (u - p).
2. Solve the energy equation (T).
3. Solve the front tracking equation F.
Check convergence. If converged goto the next time step, otherwise repeat
steps 1 to 3.
```

Steps 1 to 3 are solved using the last known values of the dependent variables and iterations are made to obtain converged solutions of the coupled system of equations.

Element matrices are constructed using a numerical Jacobian technique and assembled in a compressed sparse row format. Flow, energy and front tracking global systems are solved by BiCG stabilized iterative methods. The finite element formulations of the equations are discussed hereafter.

3.1 Flow equations

The Navier-Stokes equations (1) and (2) are solved using a Galerkin Least-Squares (GLS) method [20]. This method uses streamline upwind weight functions and contains an additional pressure stabilization term compared with the standard Galerkin method. In such a way, the use of linear elements for both the velocity and pressure is permitted. The GLS variational formulation of the momentum-continuity equations is:

$$\begin{aligned} &\int_\Omega \rho \left(\frac{\partial \mathbf{u}}{\partial t} + \mathbf{u} \cdot \nabla \mathbf{u} \right) \mathbf{v} d\Omega + \int_\Omega 2\eta \dot{\gamma}(\mathbf{u}) : \dot{\gamma}(\mathbf{v}) d\Omega - \int_\Omega p \nabla \cdot \mathbf{v} d\Omega + \int_\Omega \nabla \cdot \mathbf{u} q d\Omega \\ &+ \sum_K \int_{\Omega_K} \left\{ \rho \left(\frac{\partial \mathbf{u}}{\partial t} + \mathbf{u} \cdot \nabla \mathbf{u} \right) + \nabla p - \nabla \cdot [2\eta \dot{\gamma}(\mathbf{u})] \right\} \cdot \tau_u \left\{ \rho \mathbf{u} \cdot \nabla \mathbf{v} + \nabla q \right\} d\Omega_K = 0 \end{aligned} \tag{9}$$

where $\mathbf{v}$ and q are the velocity and pressure test functions respectively. The stabilization parameter τ_u is defined as [21,22]:

$$\tau_u = \left[\left(\frac{2\rho}{\Delta t} \right)^2 + \left(\frac{2\rho |\mathbf{u}|}{h_K} \right)^2 + \left(\frac{4\eta}{m_k h_K^2} \right)^2 \right]^{-1/2} \tag{10}$$

Here Δt is the time step, h_K is the size of the element K and m_k is a coefficient set to 1/3 for linear elements (see [20,21]).

3.2 Energy equation

The injection molding of semi-solid materials is performed at high speed and the energy equation is dominated by convection. However, cooling generated by the heat lost trough walls determines the apparition of temperature gradients in direction normal to the wall. The solution algorithm must correctly represents both advective and diffusive mechanism which have different time scales. For this reason, the energy is solved by an operator-splitting method. First the convective part of the problem is solved. Then we solve for the diffusion term. In such a way we may use particularly effective numerical schemes for each one of those problems. Moreover, the approach allows the use of fractional time steps for the advective problem which has a lower characteristic time scale than the diffusive problem. Equations to be solved are as follows:

$$\frac{T^* - T_0}{\Delta t} + \mathbf{u} \cdot \nabla T^* = 0, \tag{11}$$

$$\rho c_p \left(\frac{T - T^*}{\Delta t} \right) = \nabla \cdot (k \nabla T), \tag{12}$$

where Δt is the time step, T is the present time step temperature, T_0 is the temperature at the previous time step, and T^* is an intermediate solution of the convective problem.

The convective part solution is based on a Flux-Corrected Transport (FCT) approach [23]. The solution is constructed as from two contributions. The first one is obtained from a higher order scheme and provides numerical accuracy. Here we use a second order Taylor-Galerkin scheme:

$$\frac{T_h - T_0}{\Delta t} + \mathbf{u} \cdot \nabla T_0 - \frac{\Delta t}{2} \nabla \cdot \left[\mathbf{u} \frac{1}{2} \left(\mathbf{u} \cdot \nabla T_h + \mathbf{u} \cdot \nabla T_0 \right) \right] = 0. \tag{13}$$

The second solution comes from a lower order scheme containing additional artificial viscosity in order to avoid unphysical oscillations. In the lower order scheme the lumped mass matrix M_L is used instead of the consistent mass matrix M_C. The additional viscous term is computed as:

$$c_d (M_L - M_C) \tag{14}$$

where c_d is a coefficient given by:

$$c_d = 4 \min \left(\frac{1}{\Delta t}, 2 \frac{|\mathbf{u}|}{h_K} \right) \tag{15}$$

The FCT procedure combines the high order and the low order solutions such as the result to benefit from the accuracy of the first one and the monotonicity of the second one. Details on the procedure can be found in reference [23].

The diffusion step is solved by a Galerkin Gradient Least-Squares (GGLS) method [24]. The GGLS formulation of equation (12) is:

$$\int_\Omega \rho c_p \frac{T - T^*}{\Delta t} w \mathrm{d}\Omega + \int_\Omega k \nabla T \cdot \nabla w \mathrm{d}\Omega + \sum_K \int_{\Omega_K} \frac{\rho c_p}{\Delta t} \nabla (T - T^*) \tau_\nabla \nabla w \mathrm{d}\Omega_K = \int_{\Gamma_{mold}} h_c (T - T_{mold}) w \mathrm{d}\Gamma \tag{16}$$

Note that the stabilization term is integrated only over the element interiors. The definition of the stabilization parameter τ_∇, as from reference [24], is:

$$\tau_\nabla = \frac{h^2}{6}\bar{\xi} \tag{17}$$

where

$$\bar{\xi} = \frac{cosh(\sqrt{6\alpha}) + 2}{cosh(\sqrt{6\alpha}) - 1} - \frac{1}{\alpha} \tag{18}$$

$$\alpha = \frac{(\rho c_p/\Delta t){h_K}^2}{6k} \tag{19}$$

with h the element size. The dimensionless parameter $\bar{\xi}$ tends towards to unity for very large values of α and to 1/2 for α much smaller than the unity.

3.3 Front tracking equation

The front tracking equation is discretized using an SUPG finite element method. The variational formulation is given by

$$\int_\Omega \left(\frac{\partial F}{\partial t} + \mathbf{u}\cdot\nabla F\right) v d\Omega + \sum_K \int_{\Omega_K} \left(\frac{\partial F}{\partial t} + \mathbf{u}\cdot\nabla F\right) \tau_F(\mathbf{u}\cdot\nabla v) d\Omega_K = 0. \tag{20}$$

In the absence of diffusion the stabilization coefficient τ_F is defined as

$$\tau_F = \left[\left(\frac{2}{\Delta t}\right)^2 + \left(\frac{2|\mathbf{u}|}{h_K}\right)^2\right]^{-1/2} \tag{21}$$

The front tracking function is discretized using linear elements and reinitialized after each time step to insure mass conservation of the injected material [7].

4 Mold filling application

The application presented in this section is the injection molding of a tensile bar having $190mm$ in length. The part has a circular cross section with an initial diameter of $10mm$ on a length of $50mm$; the section diameter decreases to $6mm$ towards the middle of the part and then increases back to the same $10mm$ diameter on the last $50mm$ length. Diameter changes are gradual occurring over a length of $8mm$. The mold cavity contains four identical tensile bars. The initial flow inside the sprue separates first into two opposite flow channels and then each channel feeds two tensile bar cavities (see Figure 7). Each tensile bar is injected by one extremity and the gate makes an angle of 45^0 with the part axis, being asymmetrically located under the symmetry plane of the part to allow for part ejection. The sprue has $20mm$ in diameter and the semi-solid slurry enters the sprue at $12m/s$ ($2.5m/s$ plunger speed). The material is injected at a temperature of 580^0C and the mold is heated at 204^0C. The filling of the parts takes about $0.03s$.

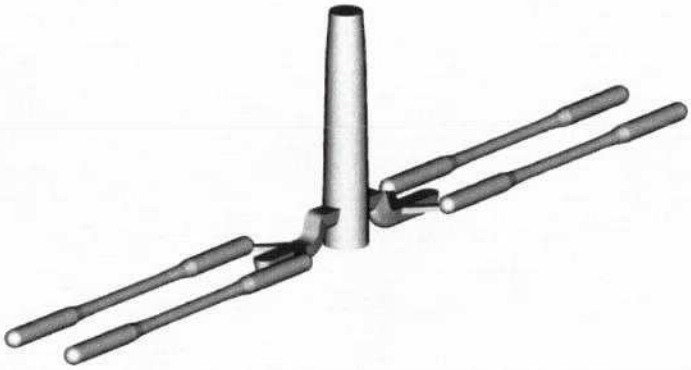

Fig. 7 Solid model for the four cavities tensile bar mold.

4.1 Experimental observations

Several series of partial (short shots) and complete fillings were carried out in order to determine the flow pattern during the filling of the experimental mold. Some of the molded parts are shown in Figure 8 for shot sizes of $28mm$, $30mm$, $32mm$ and $38mm$ respectively.

The following observations can be drawn from the the analysis of the molded parts:

- On several short shots the mold cavities were not all filled to the same extend (see Figure 8(a) and (b)). This may be caused by the fact that the mold is positioned such as the tensile bars are oriented along the vertical axis, so the gravity acts differently on the top and bottom cavities. However, the overall effect of the gravity on the filling pattern is negligible and hence it was not included in the simulation.
- The material exits the gate at high speed forming a jet that collide with the opposite wall when entering the tensile bar cavity (see Figure 8(a)). The asymmetry of the jet generates a swirling flow as the material advances along the tensile bar axis. The material fills regions near the wall and leaves empty the core of the cavity. Remark also in Figure 8(a.2), on the top left handside tensile bar, the formation of a void at the exit of the gate.
- When filling the central portion of the tensile bar (smaller diameter) the material flows mostly along the cavity wall and a void is formed along the axis of symmetry (Figure 8(b)). The void near the gate on the back side is still present on several parts.
- The material forms a jet when entering the last portion of the cavity. As can be seen in Figure 8(c), the jet goes directly towards the end of the tensile bar cavity and fills this portion of the mold from the end towards the gate. This can also be seen in Figure 8(d). The jet is quite thin and most of the $32mm$ short shots had the far end portion of the tensile bar broken from the rest of the part(see Figure 8(c)).
- The cavity seems to be filled for a shot size of $38mm$. However, at this point the material had flown mostly along the cavity walls and the parts are hollow. The complete filling is obtained for a shot size around $48mm$. Once the wall regions

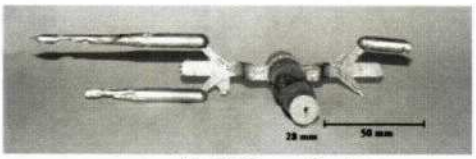

(a.1) 28mm: front view

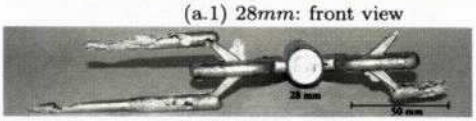

(a.2) 28mm: back view

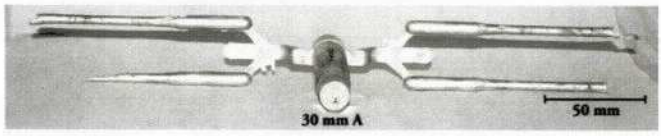

(b.1) 30mm: front view

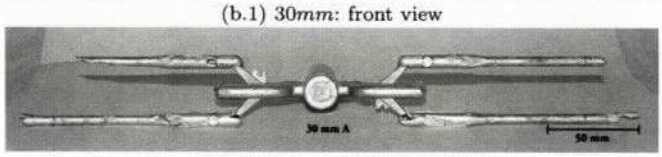

(b.2) 30mm: back view

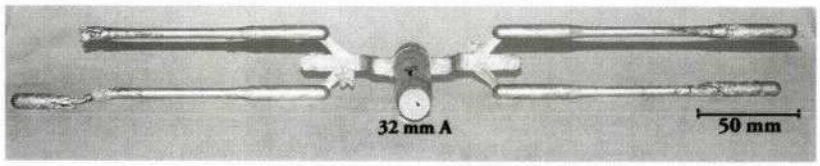

(c.1) 32mm: front view

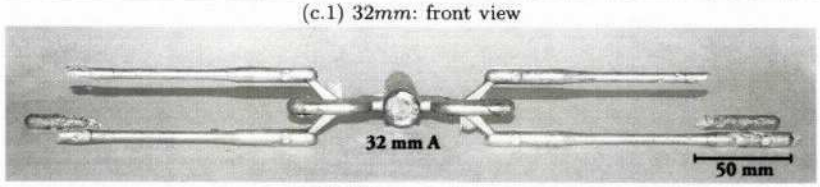

(c.2) 32mm: back view

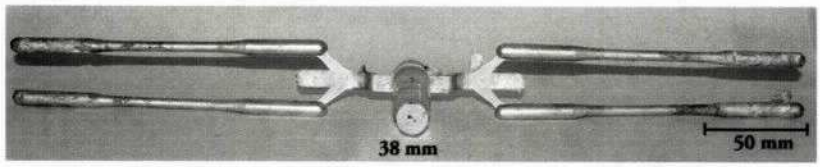

(d.1) 38mm: front view

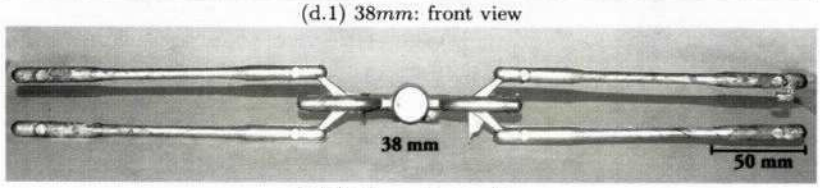

(d.2) 38mm: back view

Fig. 8 Filling pattern observed on the molded parts.

are filled, the material will fill the interior empty regions, first those near the end of the cavity and then progressively towards the gate. The last volume to be filled is located in the larger diameter region near the gate. This is confirmed by the increased porosity observed in this region.

4.2 Numerical results

Numerical simulations were carried out on a cluster of Pentium IV processors running at 3.4 GHz, connected using Myrinet-2000. Given the symmetry of the mold only a quarter of the cavity is modeled for the simulation. The mesh is formed by 354560 tetrahedral elements and has 65759 nodes. A typical transient solution for the complete mold filling contains around 2000 time steps and is computed in about 10 hours when using 32 processors.

The filling pattern is shown in Figure 9 for the viscosity model A and in Figure 10 for the viscosity model B.

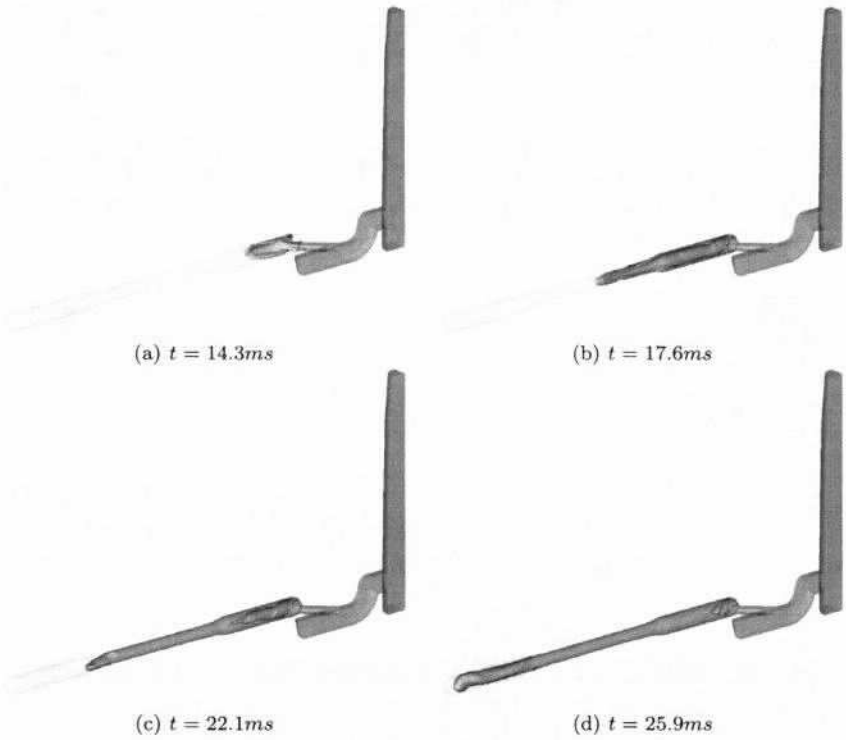

(a) $t = 14.3ms$ (b) $t = 17.6ms$

(c) $t = 22.1ms$ (d) $t = 25.9ms$

Fig. 9 Filling pattern when using the viscosity model A - Mao *et al.* [14].

The figures show the filled part of the cavity in gray scale. The filling material is shown in transparency to allow the visualization of the empty regions formed inside

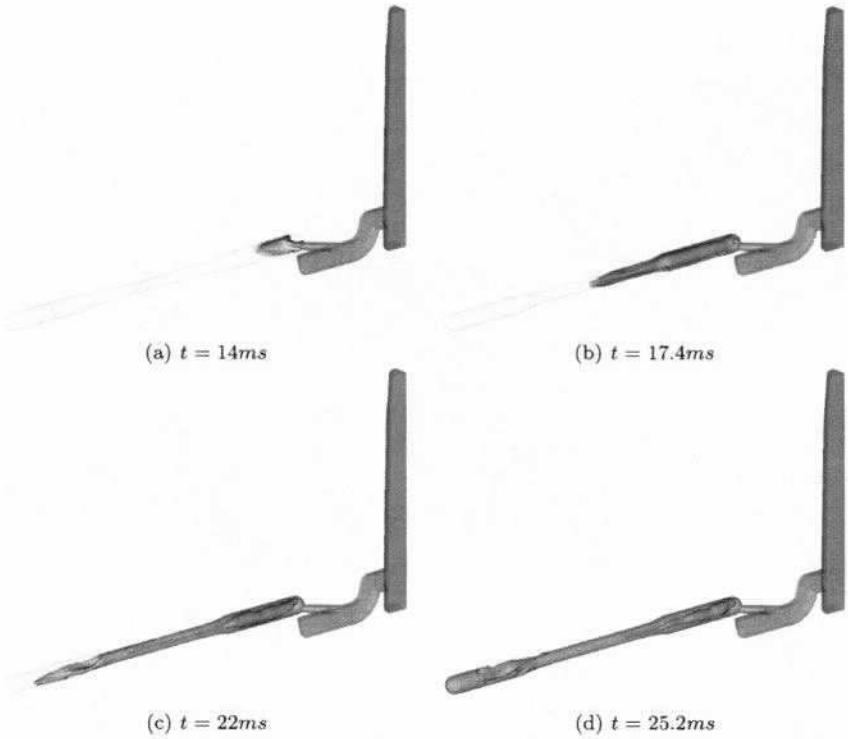

(a) $t = 14ms$ (b) $t = 17.4ms$

(c) $t = 22ms$ (d) $t = 25.2ms$

Fig. 10 Filling pattern when using the viscosity model B - Ghosh *et al.* [13].

the cavity. Flow streamlines are illustrated in Figures 11 and 12 for the simulations using the two viscosity models.

The numerical solutions indicate that the material forms a jet at the exit of the gate and a swirling flow forms as the material advances along the first larger diameter section (see streamlines in Figures 11 and 12). The wall regions are filled first, leaving a void inside. This agrees very well with the experimental observation. The first larger section remains hollow during the filling of the central smaller diameter section. In the simulation using the data of Ghosh (model B) the void continues along the center of the smaller diameter section and the material flows along the walls. This experimentally observed void is not present in the simulation using Mao's data (model A). Filling of the last larger diameter section indicates, in the case of the model B viscosity, the formation of a thinner jet that goes to the end of the cavity to complete the filling from the end towards the gate. This agrees again very well with the experimental observations. The void located in the larger section near the gate is filled last explaining the observed porosity on the molded parts.

The temperature distribution at the end of the filling is shown in Figure 13 for the solution with the lower viscosity (model B). As only a quarter of the mold cavity is modeled, the heat flux is zero along the vertical symmetry planes. Because the filling of the mold is very fast (about $30ms$) the cooling is limited and the temperature gradients

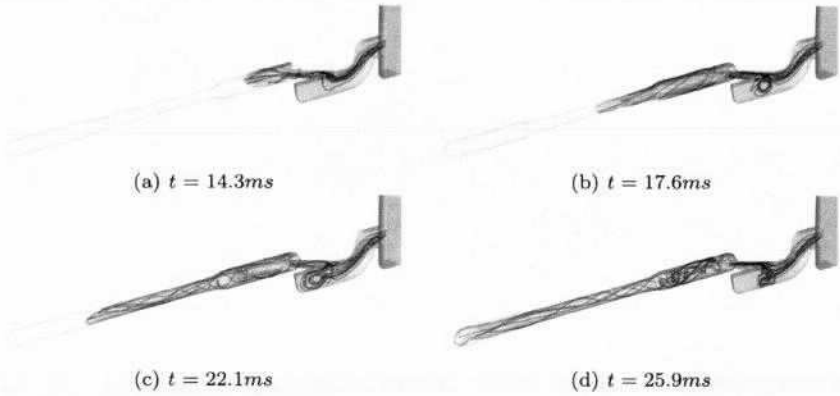

(a) $t = 14.3ms$ (b) $t = 17.6ms$

(c) $t = 22.1ms$ (d) $t = 25.9ms$

Fig. 11 Particle traces during filling when using the viscosity model A.

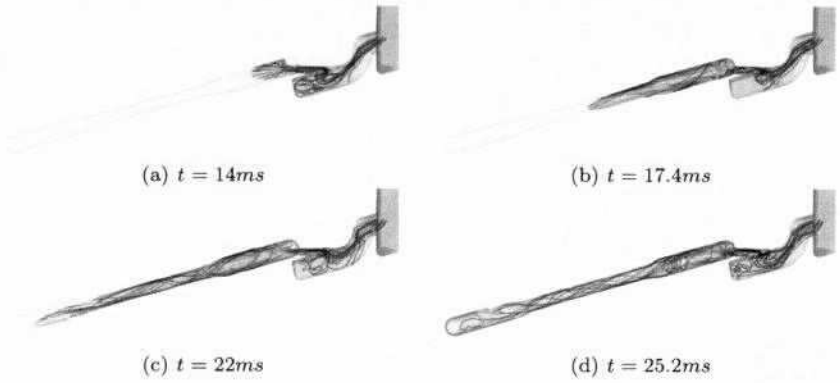

(a) $t = 14ms$ (b) $t = 17.4ms$

(c) $t = 22ms$ (d) $t = 25.2ms$

Fig. 12 Particle traces during filling when using the viscosity model B.

are relatively small. The surface temperature is smaller in the gate and along the first part of the tensile bar and increases near the end of the part.

5 Conclusion

In this paper a three-dimensional finite element algorithm is shown for the injection molding of semi-solid Mg alloys. The viscosity is described using a generalized non-Newtonian model with two sets of data. The solution algorithm is able to deal with the high Reynolds number, high shear rate flow and predicts jetting, recirculating flow and formation of voids. Both series of computations predict an important zone where porosity is likely to occur agreeing well with experimental observation. The results from the model providing a lower viscosity seems to agree better with experimental observation. Such a simulation tool could be of great help for mold makers and mold designers. It can assist the conception and production phase and help find optimum molding conditions.

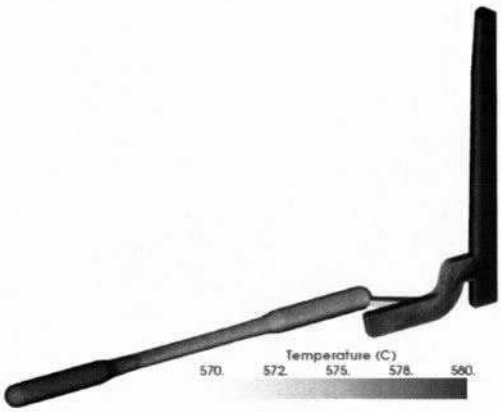

Fig. 13 Temperature distribution at the end of the filling.

References

1. R.E. Brown, "Magnesium Industry Growth in the 1990 Period," *Magnesium Technology 2000*, ed. H.I. Kaplan, J. Hryn and B. Clow, The Minerals, Metals and Materials Society, pp. 3-12, 2000.
2. A.A. Luo, "Materials Comparison and Potential Applications of Magnesium in Automobile," *Magnesium Technology 2000*, ed. H.I. Kaplan, J. Hryn and B. Clow, The Minerals, Metals and Materials Society, pp. 89-98, 2000.
3. N.L. Bradley, R.D. Weiland, W.J. Achafer, *US Patent 5040589*, 1989.
4. P.S. Frederick, N.L. Bradley, and S.C. Erickson, "Injection molding of magnesium alloys," *Advanced Materials & Processes*, vol. 134(4), pp. 53–56, 1988.
5. F. Ilinca, and J.-F. Hétu, "Finite element solution of three-dimensional turbulent flows applied to mold-filling problems," *Int. J. Num. Methods Fluids*, vol. 34, pp. 729–750, 2000.
6. F. Ilinca, and J.-F. Hétu, "Three-dimensional filling and post-filling simulation of polymer injection molding," *Int. Polym. Proc.*, vol. 16, pp. 291–301, 2001.
7. F. Ilinca, and J.-F. Hétu, "Three-Dimensional Finite Element Solution of Gas-Assisted Injection Moulding," *Int. J. Num. Methods Engng.*, vol. 53, pp. 2003–2017, 2002.
8. F. Ilinca, J.-F. Hetu, and A. Derdouri, "Numerical investigation of the flow front behavior in the co-injection molding process," *Int. J. Num. Methods Fluids*, vol. 50, pp. 1445–1460, 2006.
9. F. Ilinca, J.-F. Hetu, A. Derdouri, and J. Stevenson, "Metal Injection Molding: 3D Modeling of Nonisothermal Filling," *Polymer Engineering and Science*, vol. 42(4), pp. 760–770, 2002.
10. I.K. Kim, T.H. Kang, Y.S. Kim, Y.D. Jeong, and J.S. Kwak, "Analytical and experimental method for making magnesium alloy products based on an injection moulding process," *Int. J. Adv. Manuf. Technol.*, vol. 23, pp. 566–571, 2004.
11. A. Lohmüller, M. Scharrer, R. Jenning, M. Hilbinger, M. Hartmann, and R.F. Singer, "Injection molding of magnesium alloys," *Proc. of the 6th Int. Conf. Magnesium Alloys and Their Applications*, pp. 738–743, 2003.
12. C.D. Yim, and K.S. Shin, "Semi-solid processing of magnesium alloys," *Materials Transactions*, vol. 44(4), pp. 558–561, 2003.
13. D. Ghosh, R. Fan, and C. VanSchilt, "Thixotropic Properties of Semi-Solid Magnesium Alloys AZ91D and AM50," *Proc. of the Third Int. Conf. on Processing of Semi-Solid Alloys and Composites*, pp. 85–94, 1994.
14. C.C. Mao, J.C. Chen, H. Peng, and M.L. Chang, "Steady-state rheological behavior of semi-solid AZ91D magnesium alloy," *J. of the Chinese Soc. of Mech. Engineers*, vol. 24(4), pp. 385–389, 2003.
15. J.C. Gebelin, M. Suery, and D. Favier, "Characterisation of the rheological behavior in the semi-solid state of grain-refined AZ91D magnesium alloys," *Materials Science and Engineering*, vol. A272, pp. 134–144, 1999.

16. W.M. Mao, Z.S. Zhen, S.J. Yan, and X.Y. Zhong, "Thixotropic behavior of semi-solid AZ91D magnesium alloy," *Trans. Nonferrous Met. So. China*, vol. 14(2), pp. 297–301, 2004.
17. C.C. Yang, J.C. Fann, and H. Peng, "Investigation of rheology of magnesium semi-solid materials by using a slit rheometer," *Materials Science Forum*, vols. 419–422, pp. 623–628, 2003.
18. F. Messaoud, L. Azzi, and F. Ajersch, "Rheological characteristics of AZ91E alloys in semi-solid state," *Aluminum 2003*, Ed. S.K. Das, The Minerals, Metals & Materials Society, pp. 65-75, 2003.
19. F. Messaoud, "Charactérisations rhéologiques des alliages de magnesium a l'état semi-solide," *Ph.D. Thesis*, École Polytechnique de Montréal, 2006.
20. L.P. Franca, and S.L. Frey, "Stabilized finite element methods: II. The incompressible Navier-Stokes equations," *Comp. Methods Appl. Mech. Engng.*, vol. 99, pp. 209–233, 1992.
21. T.E. Tezduyar, R. Shih, S. Mittal, and S.E. Ray, "Incompressible flow using stabilized bilinear and linear equal-order-interpolation velocity-pressure elements," *Research Report UMSI 90/165*, University of Minnesota/Supercomputer Institute, Minneapolis, 1990.
22. F. Ilinca, J.-F. Hétu, and D. Pelletier, "On stabilized finite element formulations for incompressible flows," *13th AIAA Computational Fluid Dynamics Conference*, Snowmass, Colorado, 1997, AIAA Paper 97-1863.
23. R. Lohner, K. Morgan, J. Peraire, and M. Vahdati, "Finite Element Flux-Corrected Transport (FEM-FCT) for the Euler and Navier-Stokes equations," *Int. J. Numer. Meth. Fluids*, vol. 7, pp. 1093–1109, 1987.
24. L.P. Franca and E.G. Dutra Do Carmo, "The Galerkin gradient least-squares method," *Computer Methods in Applied Mechanics and Engineering*, vol. 74, pp. 41–54, 1989.